Computational Design of Main-Group Catalysts for Low-Temperature Methane Combustion by Ozone

Shunsaku Yasumura,[1] Kenichiro Saita,[2] Takumi Miyakage[1], Kenichi Kon[1], Takashi Toyao,[1] Zen Maeno,[3] Tetsuya Taketsugu,[2,4] Ken-ichi Shimizu*,[1]

[1] Institute for Catalysis, Hokkaido University, N-21, W-10, Sapporo 001-0021, Japan

[2] Department of Chemistry, Faculty of Science, Hokkaido University, Sapporo, Hokkaido 060-0810, Japan

[3] School of Advanced Engineering, Kogakuin University, Tokyo, 192-0015, Japan

[4] Institute for Chemical Reaction Design and Discovery (WPI-ICReDD), Hokkaido University, Sapporo, Hokkaido 001-0021, Japan

*Corresponding author

Ken-ichi Shimizu (kshimizu@cat.hokudai.ac.jp)

ABSTRACT

The catalytic combustion of methane (CH_4) at a low temperature is becoming increasingly key to controlling unburned CH_4 emissions from natural gas vehicles and power plants, although the low activity of benchmark platinum-group-metal (PGM) catalysts hinders its application. Based on the automated reaction route mapping, we designed the main-group catalyst for low-temperature CH_4 combustion with ozone (O_3). The computational screening of the active site predicted the strong Brønsted acid sites (BASs) as promising ones. We experimentally demonstrated that the catalyst comprising strong BASs exhibited improved CH_4 conversion at 200 °C, correlating with the theoretically predicted design concept. The main-group catalyst (proton-type beta zeolite) delivered a reaction rate, which was 442 times higher than that of a benchmark catalyst (5wt% Pd-loaded Al_2O_3), at 190 °C and exhibited higher tolerance to steam and SO_2. Our strategy demonstrated the rational design of earth-abundant catalysts based on automated reaction route mapping.

1. Introduction

The past decades have witnessed the widespread utilization of natural gas as a clean fuel for vehicles and power plants. The catalytic combustion of methane (CH_4) into carbon dioxide (CO_2) is becoming an increasingly valuable strategy for addressing the emissions of unburned CH_4, which exerts a greenhouse gas effect that is 22 times higher than that of CO_2.[1–3] Different types of heterogeneous catalysts, such as platinum-group-metal (PGM)- [4–7] and metal-oxide-based catalysts,[8–10] have been reported. Among them, PGM-based catalysts, such as Pd- and Pt-loaded Al_2O_3, exhibited the highest catalytic activities.[11] However, the Pd-based catalysts suffer from high operating temperatures (>500 °C) under humidity conditions, as well as irreversible deactivation by sulfation during the co-feeding of steam and SO_2.[2,12–14] Moreover, large amounts of PGMs (200–266 g) must be utilized to achieve the combustion of CH_4 in a natural-gas-fueled heavy-duty vehicle.[15] Additionally, the mining and purification of PGMs extensively impact the environment (the productions of 1 kg each of Pt and Pd generate 12,500 and 3880 kg of CO_2 equivalents, respectively). Conversely, the production of main-group elements generates significantly lower CO_2 equivalents (e.g., 8.2 kg of Al).[16,17] Thus, it is highly desirable (economically and ecologically) to develop main-group catalysts that can function at <200 °C in the co-presence of steam and SO_2.

Conventional catalyst screening, which is based on trial-and-error experiments, may not yield discontinuous discoveries, such as the main-group-facilitated catalytic combustion of CH_4 at low temperatures. The computational reaction route mapping of the unexplored chemical reaction space can benefit the discovery of different catalytic reactions.[18–23] Generally, the computations of the elementary steps in combustion reactions are considered challenging because of the abundant intermediates and products that exhibit similar formation energies and activation barriers (*Ea*).[24] To comprehensively explore the various reaction routes, density functional theory (DFT)-based automated methods for predicting reaction pathways are promising because they link the theoretical prediction to the practical designs of catalysts.[25–30] Maeda et al. developed an efficient automated path-searching method, namely the artificial force-induced reaction (AFIR) method, which involves pressing the atoms in given reactant molecules together by applying artificial force to form new structures (products) and assigning their transition states (TS).[30–41] Via AFIR, they elucidated the entire reaction pathways of uncatalyzed reactions.[32,37,39,40] The automated reaction route mapping of heterogeneous catalysis systems is still formidable owing to the complexity of the surface reactions on solid materials, where the adsorption/desorption of the reactants and products, diffusion/migration of the adsorbates, and bond rearrangements proceed simultaneously.[35,36,41]

Ozone (O_3), a strong oxidant[42], is generated onsite by a commercial ozonizer. O_3 has been employed to enhance the catalytic performance of the gas-phase combustion of volatile organic compounds (VOCs), including toluene,[43–45] acetone,[46,47] and benzene.[48,49] Regarding the combustion of CH_4 with O_3,[50–52] zeolite-based catalysts, such as Pd[53]-, Fe[54]-, Co[55]-, and proton[56]-type zeolites, have demonstrated efficiencies at low temperatures. However, the reported studies only considered the catalytic performance; thus, the strategy for designing the catalysts based on the detailed mechanism and elementary steps must still need to be addressed.

Herein, based on a computational design concept employing the AFIR method, we report a main-group catalyst for driving catalytic combustion of CH_4 with O_3 at low temperatures. First, we explored the $CH_4 + O_3$ reaction network toward generating CO_2 (Fig. 1a), confirming that the formation of methanol (CH_3OH), $CH_4 + O_3 \rightarrow CH_3OH + O_2$, was the rate-determining step (RDS) of CH_4 combustion. Thereafter, we performed the virtual screening of the active sites for RDS to propose the following concept: stronger Brønsted acid sites (BASs) exhibit higher catalytic activities (Fig. 1b). This concept was experimentally verified via CH_4 combustion tests employing O_3 at 200 °C in the presence of different BAS catalysts exhibiting different acid strengths (Fig. 1c). Finally, we demonstrated that a proton-type beta zeolite with Si/Al = 8.5 (Hß8.5) exhibited a reaction rate that was three orders of magnitude higher than that of a PGM-based benchmark catalyst, 5wt% Pd-loaded Al_2O_3 ($Pd5Al_2O_3$). The developed catalyst exhibited very high resistance to steam and SO_2 poisoning during the 170-h reaction test.

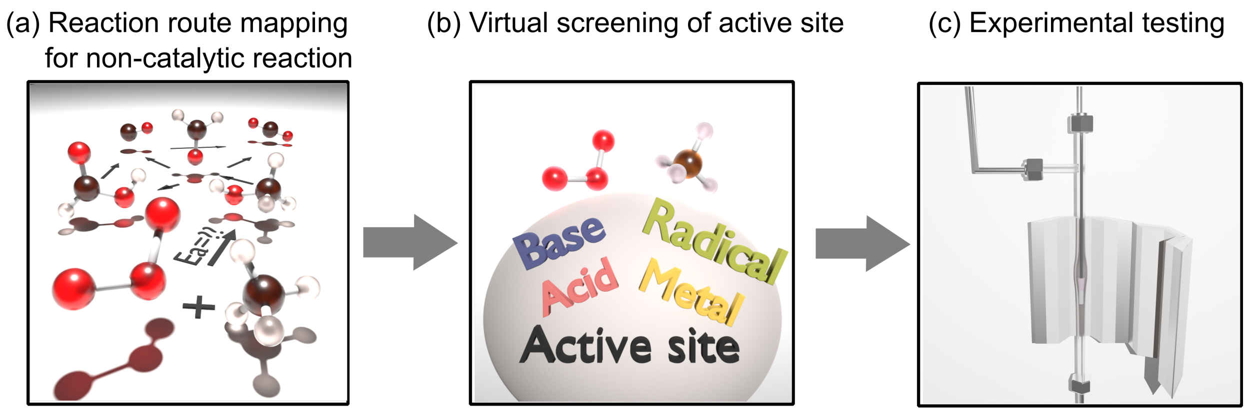

Fig. 1 Rational design concept for catalytic combustion of CH_4 with O_3. (a) Employing single-component (SC)-AFIR, CH_4 combustion with O_3 was comprehensively explored to determine the key intermediates and elementary steps. (b) Different active sites were evaluated regarding the decrease in *Ea* of the key elementary step. (c) Heterogeneous catalyst comprising the predicted active site was tested experimentally.

2. Results

2.1. Computation of the reaction pathways toward CH_4 combustion by O_3

We explored the reaction pathway of CH_4 and O_3 (CH_4 + O_3) via SC-AFIR, which was an automated method for searching for reaction paths, as implemented in the GRRM program. Employing this method, the reaction routes of the non-catalytic oxidation of CH_4 into CO_2 by O_3 are automatically mapped. Figure 2a shows the reaction pathways with the corresponding values of their relative energies (ΔE) and *Ea*s. In the first reaction, CH_4 is oxidized by O_3 to yield CH_3OH and O_2 with strong exothermicity (243.0 kJ/mol). In the TS structure, one O atom of O_3 extracts one H atom of CH_4 to yield CH_3 and OOOH fragments, where the evaluated *Ea* is 142.7 kJ/mol. This value is comparable to the reported experimental value for gas-phase CH_4 combustion by O_3 (148 kJ/mol).[57] Next, the reactivity of CH_3OH with O_3 is assessed by exploring the reaction pathway via the SC-AFIR method (see Supplementary Fig. S1). Although CH_3OH is oxidized into formaldehyde (CH_2O), H_2O, and O_2 by O_3, $CH_3OH + O_3 \rightarrow CH_2O + H_2O + O_2$, via an exothermic reaction (210.1 kJ/mol), the process requires a very high *Ea* (255.1 kJ/mol). Alternatively, the oxidation of CH_3OH by O_2 produces CH_2O and H_2O_2, $CH_3OH + O_2 \rightarrow CH_2O + H_2O_2$, via a low *Ea* of 76.1 kJ/mol (Fig. 2a). The subsequent oxidation of CH_2O by H_2O_2 yields formic acid (CH_2O_2) and H_2O, $CH_2O + H_2O_2 \rightarrow CH_2O_2 + H_2O$, with an *Ea* of 124.2 kJ/mol. The decomposition of the produced CH_2O_2 yields CO_2 and H_2, $CH_2O_2 \rightarrow CO_2 + H_2$, or CO and H_2O molecules, $CH_2O_2 \rightarrow CO + H_2O$. However, these decomposition processes require high *Ea*s to produce CO_2 and CO (264.3 and 296.3 kJ/mol, respectively) because of the high stability of CH_2O_2. As an alternative reaction path, we explored the oxidation of CH_2O by O_2, which was abundantly present in the practical systems, via SC-AFIR (see Supplementary Fig. S2). Thus, the oxidation of CH_2O by O_2 represents a facile process for producing CO and H_2O_2 via an *Ea* of 113.7 kJ/mol. The CO was oxidized into $CO_2 + O_2$ by O_3 through an *Ea* of 84.9 kJ/mol (see Supplementary Fig. S3). For comparison, Nitrous oxide (N_2O) and H_2O_2 were assessed as alternative oxidants to oxidize CH_4 into CH_3OH (see Supplementary Fig. S4). The evaluated *Ea*s of the $CH_4 + N_2O$ and $CH_4 + H_2O_2$ reactions are 269 and 177 kJ/mol, respectively, indicating that O_3 is the most efficient oxidant for producing CH_3OH.

Employing the explored reaction pathways (Fig. 2b), the reaction, $CH_4 + O_3 \rightarrow CH_3OH + O_2$, was determined as the crucial process, with the highest *Ea* in the CH_4 oxidation reaction (the RDS). To further elucidate the TS structure of this reaction, Bader charge analysis was performed to investigate the distribution of charge on each atom in the TS structure (Fig. 2b). The total atomic charges in the CH_3 fragment are almost neutral (+0.12), indicating that it is a radical-like fragment. Regarding the OOOH fragment, the structure is divided into two parts: (I) the part comprising the H and O atoms that are closer to the CH_3 fragment (denoted as O1) and (II) that comprising the other two O atoms (denoted as O2 and O3). In the former part, the determined atomic charges of the H and O1 atoms are +0.56 and −0.58, respectively, while those of the O2 and O3 atoms in the latter part are +0.06 and −0.12, respectively. This charge distribution indicates that the OOOH fragment comprises a OH radical and O_2 molecular species.

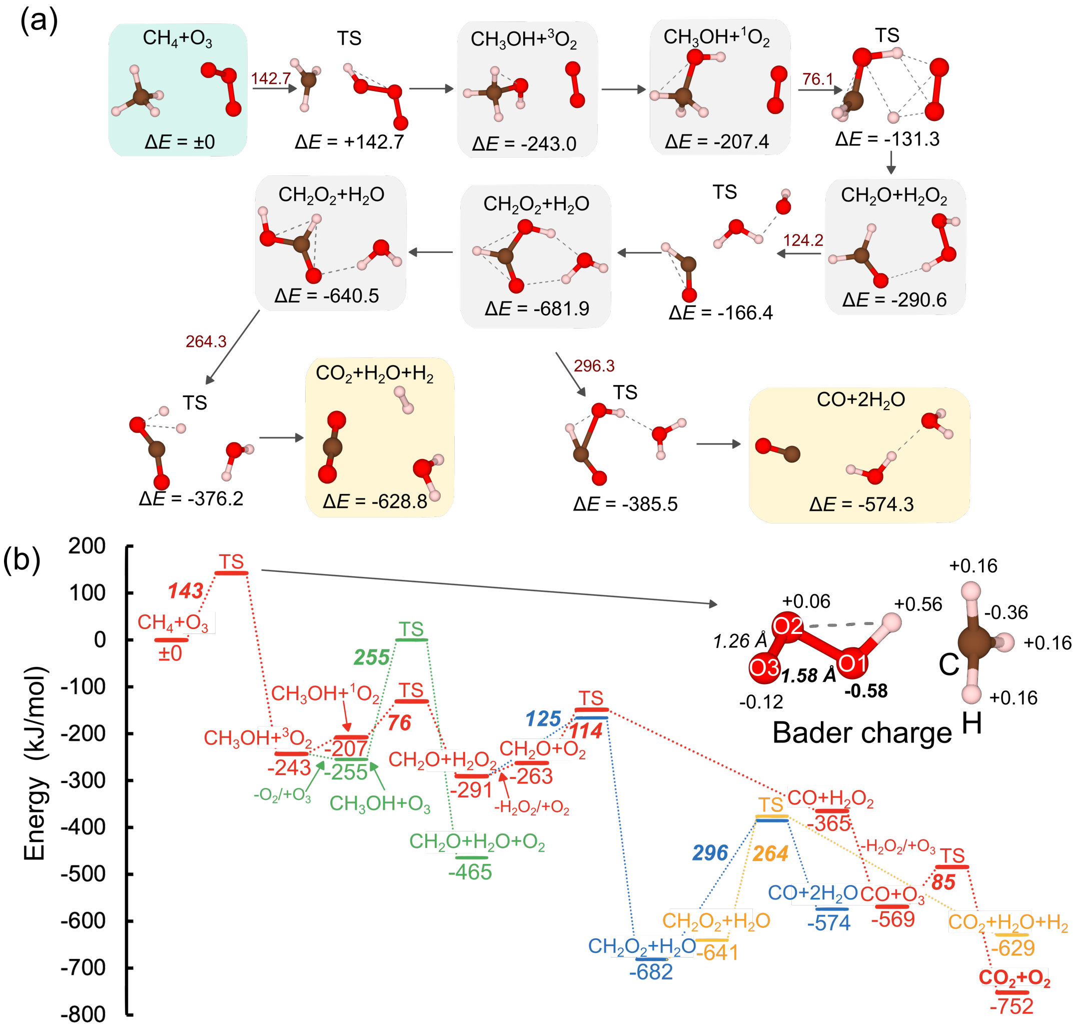

Fig. 2 (a) Calculated reaction pathway of CH_4 + O_3, as well as the values of relative energies (Δ*E*s). The values written in dark red represent *Ea*. (b) Energy profile of CH_4 combustion to yield CO_2. The reaction path shown by the red lines is the most plausible for CO_2 formation. The result of the Bader charge analyses of the TS structures of CH_4 + O_3 and CH_3OH + O_3 is shown together. Δ*E*s are provided under each bar, and the *Ea*s are described employing the bold italic style (Unit: kJ/mol)

2.2. Virtual screening of catalytic sites for the reaction of $CH_4 + O_3$ to produce $CH_3OH + O_2$

The oxidation of CH_4 by O_3 into CH_3OH and O_2 was determined as the key reaction during CH_4 combustion (Section 2.1). To conduct the virtual screening of the catalytically active sites that effectively decrease the *Ea*, we carried out SC-AFIR calculations for the $CH_4 + O_3$ reaction on the following model active sites: (a) a Cu(0) atom as a redox site, (b) an NO molecule as a radical species, (c) pyridine (C_5H_5N) as a base site, and (d) sulfuric acid (H_2SO_4) as an acid site (Fig. 3). Figure 3a shows the reaction path of $CH_4 + O_3$ over Cu(0). First, the C–H bond of CH_4 is cleaved by the O atom of O_3 over the Cu atom to yield OH and CH_3 groups on the Cu(II) cation (Cu(OH)(CH_3)), as well as adsorbed O_2 molecules through a high *Ea* (318.2 kJ/mol). Subsequently, the adsorbed O_2 molecule interacts with the neighboring CH_3 group to form CH_3OO species on the Cu(II) cation (Cu(OH)(CH_3OO)) via an *Ea* of 115.4 kJ/mol, while the extraction of the H atom of the OH group (Cu(O)(OOH)(CH_3)) is determined as an unfavorable path. Finally, the $Cu(OH)_2$ species and CH_2O are produced with a moderate barrier (108.7 kJ), although the Cu(II) cation was not reduced back into the Cu(0) atom. The maximum barrier was higher than that of the uncatalyzed reaction (142.7 kJ/mol). Hence, the Cu(0) atom was not a suitable catalyst for the $CH_4 + O_3$ reaction. Further, the NO molecules as a representative radical site reacted with O_3 to yield O_2 and NO_2, where the H atom of CH_4 was subsequently extracted to yield the CH_3 radical species that were bound to the nitrous acid (HONO) species (Fig. 3b). Although the evaluated *Ea* of this step was relatively low (122.7 kJ/mol), that of the reverse reaction (CH_3• + HONO → $CH_4 + NO_2$) was very low (2.0 kJ/mol). Additionally, the reaction, $NO_2 + CH_4$, to yield $CH_3OH + O_2$ shows only a low exothermicity (−21.1 kJ/mol). These results indicate that NO is also an inefficient catalyst for the $CH_4 + O_3$ reaction. In the case of C_5H_5N as a base site, O_3 slightly interacted with the basic site (the N atom) of C_5H_5N before reacting with CH_4; thus, O_3 was not decomposed by the active site (Fig. 3c). Thereafter, CH_3OH was produced through a similar TS structure to the gas-phase one, and the product, which was weakly bound to the base site, was slightly more stable than that in the gas phase ($\Delta E = -264$ kJ (on the base site) vs −243 kJ (in the gas phase)), while their *Ea*s were comparable (*Ea* = 134.9 vs 142.7 kJ/mol). Finally, H_2SO_4 was assessed as an acid site. CH_3OH was produced via an *Ea* of 126.2 kJ/mol, which was lower than that of the gas-phase reaction (142.7 kJ/mol), with very high exothermicity ($\Delta E = -279.3$ kJ/mol; Fig. 3d). Consequently, we predicted that BASs were the most effective among the virtually screened active sites for $CH_4 + O_3$. In the next section, we discussed the preferable property of BAS, as well as the detailed mechanism of decreasing *Ea*.

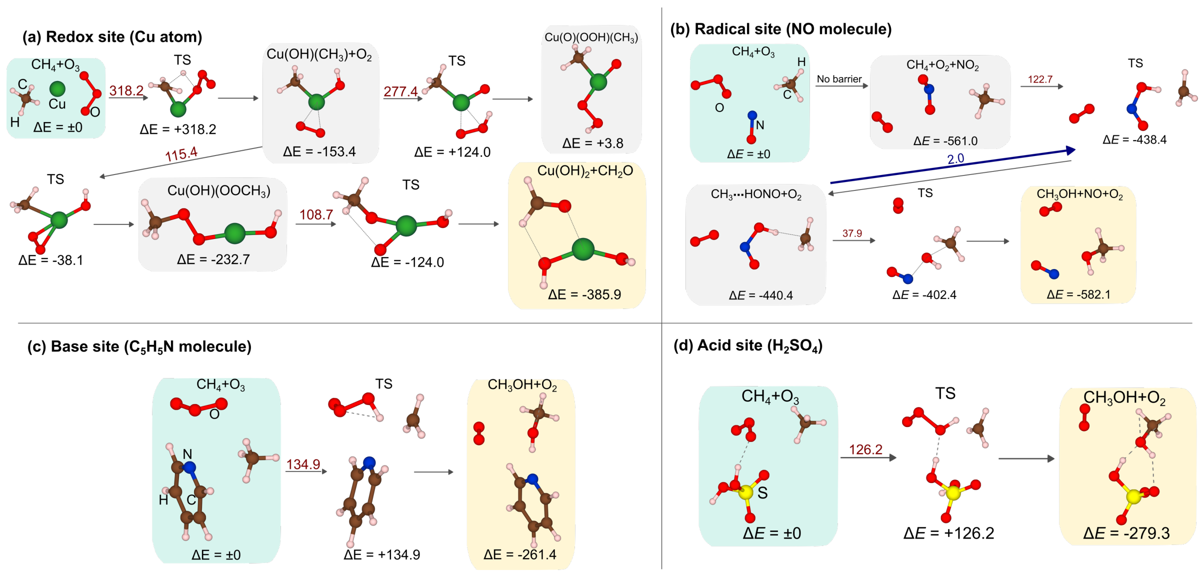

Fig. 3 Calculated reaction pathways of CH_4 + O_3 on (a) Cu(0) atom, (b) NO molecule, (c) C_5H_5N molecule, and (d) H_2SO_4 molecule. The values of Δ*E* and the *Ea* (dark red) are shown together (Unit: kJ/mol)

2.3. Promotion effect of BAS on the CH_4 + O_3 reaction

We investigated the effect of the acid strength of BASs of the mineral acids on the *Ea* of CH_4 + O_3. H_2SO_4, perchloric acid ($HClO_4$), nitric acid (HNO_3), and phosphoric acid (H_3PO_4) were evaluated as BASs exhibiting different acidities. The initial structure (IS), final structure (FS), and TS are shown in Supplementary Fig. S5. The *Ea*s of the strong acids (128.4 and 126.2 kJ/mol for $HClO_4$ and H_2SO_4, respectively) are lower than that of the uncatalyzed reaction (142.7 kJ/mol), which is close to the value for a weak acid (142.2 and 138.8 kJ/mol for H_3PO_4 and HNO_3, respectively).

To quantitatively evaluate the impact of the acid strength, the *Ea*s of the CH_4 + O_3 reaction are plotted as a function of the stabilization energy of C_5H_5N on BASs (E_{pyr}), as determined by DFT calculations. Notably, the adsorption of C_5H_5N on BAS of solid material has been widely applied to experimentally and theoretically analyze its acidity.[58–60] The values of E_{pyr} for $HClO_4$, H_2SO_4, HNO_3, and H_3PO_4 are −94.3, −91.1, −70.9, and −76.2 kJ/mol, respectively, indicating that the stronger acids ($HClO_4$ and H_2SO_4) avail a more stable structure than the weaker acids (HNO_3 and H_3PO_4), corresponding to their experimentally obtained deprotonation enthalpies (see Supplementary Table S1). Figure 4d shows that the *Ea*s of the CH_4 + O_3 reaction on BASs decreased with the increasing acid strengths, indicating that stronger BASs correspond to higher reaction rates for the CH_4 + O_3 reaction. Bader charge analysis was performed on the TS structures of the examined acids (see Supplementary Figure S6). The charge of the O atom in the OH species of the strong acids (−0.70) is more negative than those of the two weak acids (−0.66 and −0.62). Regarding the bond distance in the TS structure, the more negative charge of the O atom elongates the O–O bond in the OOOH fragment (1.69 vs. 1.66 Å for $HClO_4$ and H_3PO_4, respectively), thereby decreasing *Ea*.

Inspired by the newly gained insight into BASs as active sites, a proton-type zeolite (ß-type) was theoretically examined for the adsorption of C_5H_5N (Figs. 4a and b). The result indicates the higher acid strength of the zeolite (E_{pyr} = −199.8 kJ/mol) than that of H_2SO_4 (−91.1 kJ/mol). The extrapolation of the linear relationship between

E_{pyr} and *Ea* of the mineral acids indicates that the zeolite might achieve an extremely low *Ea* (~60 kJ/mol). To verify this hypothesis, we conducted TS calculations for the $CH_4 + O_3$ reaction on the BAS of the zeolite. Figure 4c shows the optimized structures of IS, TS, and FS. As expected from the strong acidity of the zeolite, the computed *Ea* (71.2 kJ/mol) is considerably lower than those for the mineral acids (126.2–142.2 kJ/mol).

Next, we experimentally verified the theoretically predicted relationship between the *Ea* and acid strength (E_{pyr}) of the $CH_4 + O_3$ reaction. The mineral acid (3 wt% H_2SO_4, $HClO_4$, HNO_3, or H_3PO_4) was loaded onto an SiO_2 support and tested for the reaction in a 0.1% CH_4 + 5.95% O_2 + 0.7% O_3 + 3% H_2O flow (total flow: 100 ml/min, He balance) at 200 °C employing a fixed-bed flow reactor. The concentrations of CH_4 and O_3 in the outlet gas were monitored by a gas cell that was equipped with an infrared spectroscope (Supplementary Fig. S7 shows the illustration of the experimental setup). The observed conversions of CH_4 are plotted as a function of E_{pyr} (Figure 4e). Interestingly, the observed conversions of CH_4 correlate moderately with E_{pyr}. Next, an Hß zeolite with a relatively low Si/Al ratio (8.5) (Hß8.5) was tested via the same reaction. Therein, Hß8.5 achieves an extremely higher conversion of CH_4 (97%) than $HClO_4$ (23%), demonstrating the highest CH_4 conversion among the tested catalysts. The above results demonstrate that the high CH_4-combustion activity of a strong BAS-based catalyst, Hß8.5, could be rationally predicted based on computational mapping of the reaction network, as well as TS calculations. In the next section (2.4), we experimentally demonstrate the superior performance of Hß8.5 by comparing it with $Pd5Al_2O_3$ as a conventional catalyst.

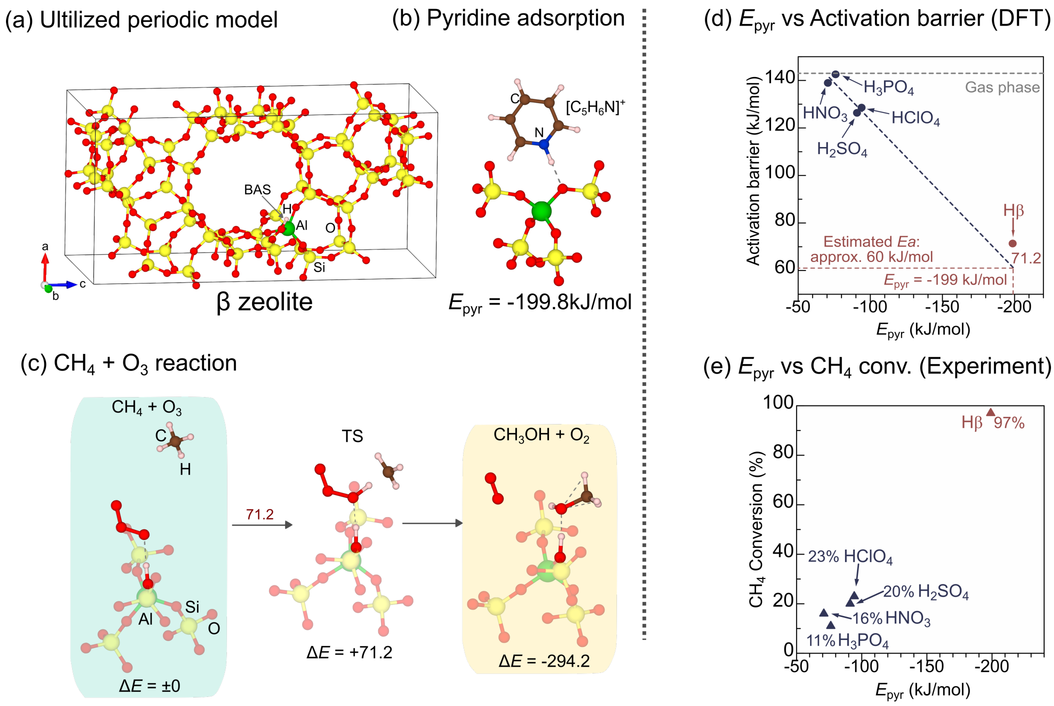

Fig. 4 (a) Employed periodic model of the ß zeolite. (b) Structure of the adsorption of C_5H_5N on BAS of ß zeolite. (c) TS calculations of the $CH_4 + O_3$ reaction on BAS of the ß zeolite. ΔE is reported in the kJ/mol unit. *Ea* is shown in dark red. (d) Plot of *Ea* of the $CH_4 + O_3$ reaction as a function of the C_5H_5N-stabilization energy (E_{pyr}) of the acids. (e) CH_4 conversion of 40 mg of the samples in 0.1% CH_4 + 5.95% O_2 + 0.7% O_3 + 3% H_2O at 200 °C (He balance, total flow: 100 ml/min) as a function of E_{pyr}

2.4. Performance of the Hß-catalyzed CH_4 combustion with O_3

We conducted catalytic tests to experimentally demonstrate the catalytic performance of Hß8.5. Figure 5a shows the conversions of CH_4 over Hß8.5 and a benchmark catalyst ($Pd5Al_2O_3$) in a flow of 0.1% CH_4 + 5.95% O_2 + 0.7% O_3 at different temperatures. In 0.1% CH_4 + 10% O_2, Hß8.5 did not achieve CH_4 conversion in the entire temperature range, indicating the necessity of O_3 as the oxidant. In 0.1% CH_4 + 5.95% O_2 + 0.7% O_3, Hß8.5 achieved the high conversion of CH_4 at 200 °C, while $Pd5Al_2O_3$ required a temperature of >400 °C to achieve comparable performance. At >250 °C, the conversion of CH_4 over Hß8.5 decreased because O_3 conversion had reached 100% via self-decomposition (Fig. 5b). The effect of BAS on the self-decomposition of O_3 into O_2 ($2O_3 \rightarrow 3O_2$) was theoretically investigated because this reaction represented an obstacle to the practical application of O_3 as an oxidant. Supplementary Fig. S8 shows the comparison between the optimized TS structures of the uncatalyzed and Hß-catalyzed decompositions of O_3. The calculated *Ea* of the uncatalyzed and Hß-catalyzed reactions are 42.3 and 69.5 kJ/mol, respectively, indicating that BAS in zeolite do not promote the self-decomposition of O_3. This property is desirable in catalysts for CH_4 combustion by O_3. Dissimilar to Hß8.5, $Pd5Al_2O_3$ exhibited high activity toward O_3 decomposition (complete conversion even at 50 °C); hence, the addition of O_3 did not increase the CH_4 combustion activity of $Pd5Al_2O_3$.

Figure 5c shows a plot of the conversions of CH_4 and O_3, as well as the BAS amounts, as evaluated by NH_3-adsorption measurement as a function of the Si/Al ratio of the utilized ß zeolites (Si/Al = 8.5, 12.5, 20, and 255). Evidently, the Al-rich ß zeolites with more BASs exhibited higher CH_4 conversions. The Arrhenius plot of the Hß8.5-catalyzed CH_4 combustion with O_3 (Fig. 5d) revealed an apparent barrier (*E*a) of 75 kJ/mol, which agrees with the theoretical value of the CH_4 + O_3 reaction to yield CH_3OH (*E*a = 71.2 kJ/mol). The *E*a of Hß8.5 was considerably lower than that of $Pd5Al_2O_3$ (*E*a = 95 kJ/mol) in 0.1% CH_4 + 10% O_2. Supplementary Fig. S9 shows the results of the kinetic analyses for estimating the reaction orders. The reaction orders of CH_4 (0.2) and O_3 (0.2) were positive. Further, the reaction rates per weight of the catalyst (for Hß8.5 and $Pd5Al_2O_3$) for CH_4 conversion (V_{CH4}) at 190 °C were compared, and the result indicated that V_{CH4} of Hß8.5 (57.5 mmol h^{-1} g_{cat}^{-1}) was 442 times higher than that of $Pd5Al_2O_3$ (0.13 mmol h^{-1} g_{cat}^{-1}), demonstrating that the designed main-group catalyst (Hß8.5) exhibited considerably higher activity toward CH_4 combustion than the PGM-based benchmark catalyst.

Further, Hß8.5 and $Pd5Al_2O_3$ were tested for CH_4 combustion in the co-presence of H_2O and SO_2 to compare their resistance to steam and SOx poisoning. Figure 5f shows the time course of CH_4 combustion over 40 mg of Hß8.5 (5.95% O_2 + 0.7% O_3 at 200 °C) and $Pd5Al_2O_3$ (10% O_2 at 400 °C) in 0.1% CH_4 + 3% H_2O + 40 ppm SO_2. By feeding H_2O and SO_2, the CH_4 conversion at 400 °C over $Pd5Al_2O_3$ decreased with the reaction time, reaching almost zero after 10 h. Conversely, the CH_4 conversion over Hß8.5 did not decrease at 200 °C even after 15 h, indicating that Hß8.5 was highly resistant to steam and SO_2 poisoning. Finally, 10 mg of Hß8.5 was examined for the long-term reaction test in 0.1% CH_4 + 5.95% O_2 + 0.7% O_3 + 3% H_2O + 40 ppm SO_2 at 200 °C, and the result indicated that the catalyst did not significantly decrease the CH_4 conversion for 170 h of reaction time.

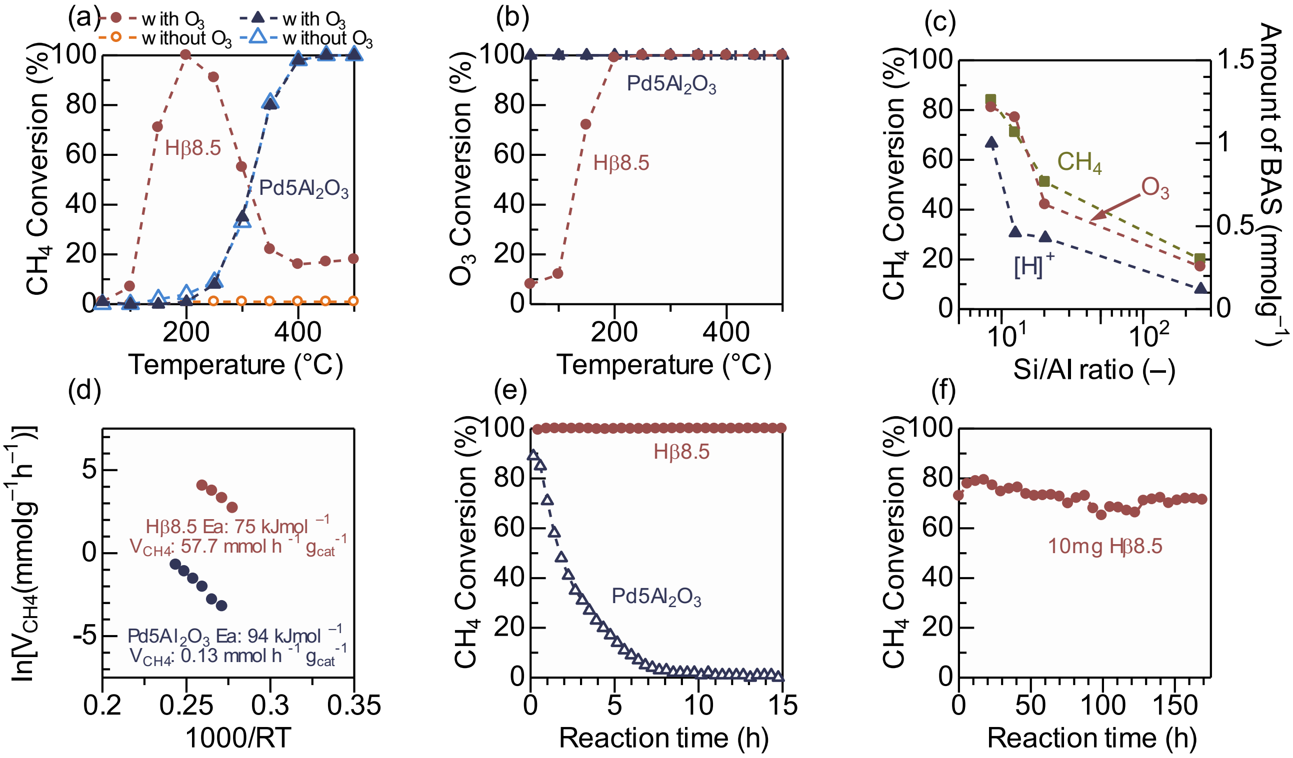

Fig. 5 (a) CH_4 and (b) O_3 conversions over 40 mg of the Hß zeolite with an Si/Al ratio of 8.5 (Hß8.5) and 40 mg of 5 wt% Pd-loaded Al_2O_3 ($Pd5Al_2O_3$) in 0.1% CH_4 + 5.95% O_2 + 0.7% O_3 and 0.1% CH_4 + 10% O_2 flows as functions of the reaction temperature. (c) Conversions of CH_4 and O_3 over 40 mg of the Hß zeolite with different Si/Al ratios (8.5, 12.5, 20, and 255) in a 0.1% CH_4 + 5.95% O_2 + 0.7% O_3 flow at 150 °C, together with the amount of BAS in the ß zeolite, as evaluated via NH_3-adsorption measurements. (d) Arrhenius plots for the combustions of CH_4 over Hß8.5 in 0.1% CH_4 + 5.95% O_2 + 0.7% O_3 at 160–190 °C, as well as over $Pd5Al_2O_3$ in 0.1% CH_4 + 10% O_2 at 170–220 °C. The reaction rates (V_{CH4}) at 190 °C over Hß8.5 and $Pd5Al_2O_3$ are shown together (R^2 = 0.99 for both catalyst). (e) Time course of CH_4 conversion over 40 mg of $Pd5Al_2O_3$ (at 400 °C) and Hß8.5 (at 200 °C) in 0.1% CH_4 + 3% H_2O + 40 ppm SO_2 + 10% O_2 or 5.95% O_2 + 0.7% O_3 for $Pd5Al_2O_3$ and Hß8.5, respectively, with He balance (total flow: 100 ml/min). (f) Long-term reaction test for 10 mg of Hß8.5 in 0.1% CH_4 + 5.95% O_2 + 0.7% O_3 + 3% H_2O + 40 ppm SO_2 at 200 °C

Discussion

In this study, we rationally designed a catalyst for low-temperature O_3-driven catalytic combustion of CH_4 based on the elucidation of an unexplored reaction network. The CH_4 + O_3 reaction toward generating CO_2 was explored via SC-AFIR, and the formation of CH_3OH via CH_4 + O_3 ($CH_4 + O_3 \rightarrow CH_3OH + O_2$) was determined as RDS of CH_4 combustion (Ea = 142.7 kJ/mol). To assess the various types of active sites (acid, base, redox, and radical sites), model molecules (H_2SO_4, C_5H_5N, a Cu atom, and HNO_3) were introduced into the system, and reaction route was calculated. Among the examined active sites, H_2SO_4 effectively decreased the reaction (Ea = 126.2 kJ/mol); thus, different Brønsted acid catalysts with different acid strengths were examined for the TS calculation. The relationship between the acidity and calculated Ea of the CH_4 + O_3 reaction (CH_3OH formation) availed a facile catalyst design concept; the stronger the BASs afford the higher the catalytic activity. Thereafter, the theory-driven concept was experimentally verified by CH_4 combustion with O_3 at 200 °C. An Hß zeolite, which was the most effective candidate, as predicted by this concept, was experimentally tested for the CH_4 + O_3 reaction. The apparent activation energy (75 kJ/mol), which was estimated by the kinetic experiment, was consistent with the computed value (71.2 kJ/mol). Hß exhibited a very high reaction rate, which was 442 times higher than that of the benchmark catalyst, $Pd5Al_2O_3$, at 190 °C. During the catalytic tests in the presence of SO_2 and H_2O, Hß achieved the full conversion of CH_4 at 190 °C, whereas $Pd5Al_2O_3$ was completely deactivated even at a higher temperature (400 °C) owing to the poisoning of its active sites by water and SO_2. Finally, the developed catalyst (Hß zeolite) was tested in a 170-h long-term reaction in which it exhibited very high resistance against water and SO_2. These results demonstrated that a computationally designed catalyst based on earth-abundant metal elements (Si and Al) could achieve higher activities and durabilities compared with their PGM-based counterparts for the unprecedented low-temperature CH_4 combustion. A further improvement of the catalytic performance based on automated reaction route mapping is in progress.

Method

DFT calculations

Spin-polarized DFT calculations were performed employing the generalized-gradient approximation of Perdew–Burke–Ernzerhof (GGA-PBE) functional,[61] as implemented in the Vienna Ab Initio Simulation Package[62,63] (VASP), and the projected augmented waves[64,65] (PAW) method was employed for the Kohn–Sham equations with cut-off energy of 500 eV. The Γ point was employed for the Brillouin-zone sampling[66]. DFT-D3 dispersion correction with the Becke–Johnson damping was employed for all the calculations[67]. To simulate the gas-phase reaction, calculations were conducted within a large cubic cell ($a = b = c$ = 15 Å). The structure of the β zeolite was obtained from the International Zeolite Association (IZA) database,[68] and the lattice constants were fixed at initial values ($a = b$ = 12.632 Å, c = 26.186 Å, $\alpha = \beta = \gamma$ = 90.0°) during the calculations. The SC-AFIR method, as implemented in the GRRM17 program,[38] was applied for reaction route mapping with a model collision energy parameter of 1000 kJ/mol. Only a positive force was applied for the AFIR calculations. The H, O, and C atoms in the CH_4 and O_3 molecules were considered the targets of SC-AFIR. The locally updated plane (LUP) method availed the path top (PT) points, which were subsequently optimized as TS structures and determined by the following intrinsic reaction coordinate (IRC) calculation.[69] To calculate for the β zeolite, the atoms of the zeolitic framework, except for the Al atom, as well as the Si atoms adjacent to the Al and O atoms connecting to the adjacent Si, and H atoms of BAS were fixed at the crystallographic position (Figure 5b). The stabilization energy of C_5H_5N was defined, as follows:

$$E_{\mathrm{pyr}} = (E_{\mathrm{C5H5N\ on\ BAS}} - E_{\mathrm{BAS}} - E_{\mathrm{C5H5N}})$$

Thus, the total energies of the models including a C_5H_5N molecule, acid molecules, and C_5H_5N interacting with the acid molecules were described as E_{C5H5N}, E_{BAS}, and $E_{\mathrm{C5H5N\ on\ BAS}}$, respectively.

Experiments

Proton-type (H) β zeolite with a Si/Al ratio of 8.5 (Hβ 8.5) was obtained via the calcination of an NH_4^+-type β zeolite that was purchased from Tosoh Co. (HSZ-920NHA) in the air at 500 °C. The Hβ zeolites with Si/Al ratios of 20 and 255 (HSZ-940HOA and HSZ-980HOA, respectively) were supplied by Tosoh Co., and another with a Si/Al ratio of 12.5 was supplied by the Catalysis Society of Japan (JRC-Z-HB25). Acid-load SiO_2 was prepared via impregnation method. SiO_2 (CARiACT Q–10, Fuji Silysia) was suspended in an aqueous solution of H_2SO_4, $HClO_4$, H_3PO_4, and HNO_3. The water was evaporated form the mixture and dried in an oven. Al_2O_3 was prepared by calcining γ-AlOOH (Catapal B Alumina, Sasol) for 3 h at 900 °C. Next, 5 wt% Pd-loaded Al_2O_3 was prepared by impregnating Al_2O_3 with an aqueous HNO_3 solution of $Pd(NH_3)_2(NO_3)_2$. The catalytic test was conducted in a fixed-bed reactor under in 0.1% CH_4 + 0.7% O_3 + 5.95% O_2 (He balance, total flow:100 ml/min) as a typical condition. The outlet was directly connected to a JASCO FT/IR-4600 spectrometer that was equipped with a triglycine sulfate (TGS) detector, in which a homemade infrared (IR) gas cell, which was equipped with KBr windows, was placed to monitor the concentrations of CH_4 and O_3. The IR area of O_3 was calibrated employing an O_3 analyzer (EG-550, EcoDesign Inc.) to convert the area into concentration. To feed O_3 into the system, an O_2 flow was passed through an ozonizer (F0G-AC5G, EcoDesign Inc.) that was placed before the mainstream. The whole view of the employed setup is shown in Supplementary Figure S7. The NH_3-adsorption measurement was carried out by Infrared spectroscopy (JASCO FT/IR-4200 spectrometer using a home-made *in situ* IR cell. The catalyst disc of the zeolite sample (40 mg,) was dehydrated under He flow at 500 °C before a background spectrum was recorded under a flow of He at 200 °C. Then, NH_3 (1%) flowed to the sample, followed by He purging bwfore IR spectrum was taken at 200 °C.

Data availability:

The data, which support the result in this study, can be found in the manuscript and Supplementary information. They are available from the corresponding author upon reasonable request.

Reference

1. Petrov, A. W. *et al.* Stable complete methane oxidation over palladium based zeolite catalysts. *Nature Communications* **9**, (2018).
2. Petrov, A. W., Ferri, D., Tarik, M., Kröcher, O. & van Bokhoven, J. A. Deactivation Aspects of Methane Oxidation Catalysts Based on Palladium and ZSM-5. *Topics in Catalysis* **60**, 123–130 (2017).
3. Jiang, D., Khivantsev, K. & Wang, Y. Low-Temperature Methane Oxidation for Efficient Emission Control in Natural Gas Vehicles: Pd and beyond. *ACS Catalysis* **10**, 14304–14314 (2020).
4. Mahara, Y., Tojo, T., Murata, K., Ohyama, J. & Satsuma, A. Methane combustion over Pd/$CoAl_2O_4$ /Al_2O_3 catalysts prepared by galvanic deposition. *RSC Advances* **7**, 34530–34537 (2017).
5. Colussi, S., Fornasiero, P. & Trovarelli, A. Structure-activity relationship in Pd/CeO_2 methane oxidation catalysts. *Chinese Journal of Catalysis* **41**, 938–950 (2020).
6. Xiong, H. *et al.* Engineering catalyst supports to stabilize PdO_x two-dimensional rafts for water-tolerant methane oxidation. *Nature Catalysis* **4**, 830–839 (2021).
7. Losch, P. *et al.* Modular Pd/Zeolite Composites Demonstrating the Key Role of Support Hydrophobic/Hydrophilic Character in Methane Catalytic Combustion. *ACS Catalysis* **9**, 4742–4753 (2019).
8. Arai, H., Yamada, T., Eguchi, K. & Seiyama, T. Catalytic combustion of methane over various perovskite-type oxides. *Applied Catalysis* **26**, 265–276 (1986).
9. Ferri, D. & Forni, L. Methane combustion on some perovskite-like mixed oxides. *Applied Catalysis B: Environmental* **16**, 119–126 (1998).
10. Tao, F. F. *et al.* Understanding complete oxidation of methane on spinel oxides at a molecular level. *Nature Communications* **6**, (2015).
11. He, L., Fan, Y., Bellettre, J., Yue, J. & Luo, L. A review on catalytic methane combustion at low temperatures: Catalysts, mechanisms, reaction conditions and reactor designs. *Renewable and Sustainable Energy Reviews* **119**, (2020).
12. Goodman, E. D. *et al.* Catalyst deactivation via decomposition into single atoms and the role of metal loading. *Nature Catalysis* **2**, 748–755 (2019).
13. Yang, W. *et al.* A Review on the Impact of SO_2 on the Oxidation of NO, Hydrocarbons, and CO in Diesel Emission Control Catalysis. *ACS Catalysis* **11**, 12446–12468 (2021).
14. Hou, Z. *et al.* Electronically Engineering Water Resistance in Methane Combustion with an Atomically Dispersed Tungsten on PdO Catalyst. *Angewandte Chemie International Edition* **61**, (2022).
15. Keenan, M. *et al.* The Catalytic Challenges of Implementing a Euro VI Heavy Duty Emissions Control System for a Dedicated Lean Operating Natural Gas Engine. *Topics in Catalysis* **62**, 273–281 (2019).
16. Nuss, P. & Eckelman, M. J. Life cycle assessment of metals: A scientific synthesis. *PLoS ONE* **9**, 1–12 (2014).
17. Bullock, R. M. *et al.* Using nature's blueprint to expand catalysis with Earth-abundant metals. *Science (1979)* **369**, (2020).
18. Stocker, S., Csányi, G., Reuter, K. & Margraf, J. T. Machine learning in chemical reaction space. *Nature Communications* **11**, 1–11 (2020).
19. Kreitz, B. *et al.* Quantifying the Impact of Parametric Uncertainty on Automatic Mechanism Generation for

CO_2 Hydrogenation on Ni(111). *JACS Au* **1**, 1656–1673 (2021).

20. Lan, T. & An, Q. Discovering Catalytic Reaction Networks Using Deep Reinforcement Learning from First-Principles. *J Am Chem Soc* **143**, 16804–16812 (2021).
21. Nakao, A., Harabuchi, Y., Maeda, S. & Tsuda, K. Leveraging algorithmic search in quantum chemical reaction path finding. *Physical Chemistry Chemical Physics* **24**, 10305–10310 (2022).
22. Xu, J., Cao, X. M. & Hu, P. Perspective on computational reaction prediction using machine learning methods in heterogeneous catalysis. *Physical Chemistry Chemical Physics* **23**, 11155–11179 (2021).
23. Fu, X., Li, J., Long, J., Guo, C. & Xiao, J. Understanding the Product Selectivity of Syngas Conversion on ZnO Surfaces with Complex Reaction Network and Structural Evolution. *ACS Catalysis* **11**, 12264–12273 (2021).
24. He, Z., Li, X. B., Liu, L. M. & Zhu, W. The intrinsic mechanism of methane oxidation under explosion condition: A combined ReaxFF and DFT study. *Fuel* **124**, 85–90 (2014).
25. Hannagan, R. T. *et al.* First-principles design of a single-atom – alloy propane dehydrogenation catalyst. **4**, 1444–1447 (2021).
26. Ulissi, Z. W., Medford, A. J., Bligaard, T. & Nørskov, J. K. To address surface reaction network complexity using scaling relations machine learning and DFT calculations. *Nature Communications* **8**, 1–7 (2017).
27. Latimer, A. A. *et al.* Understanding trends in C-H bond activation in heterogeneous catalysis. *Nature Materials* **16**, 225–229 (2017).
28. Schweitzer, J.-M. *et al.* Multiscale Modeling as a Tool for the Prediction of Catalytic Performances: The Case of n -Heptane Hydroconversion in a Large-Pore Zeolite. *ACS Catalysis* **12**, 1068–1081 (2022).
29. Bruix, A., Margraf, J. T., Andersen, M. & Reuter, K. First-principles-based multiscale modelling of heterogeneous catalysis. *Nature Catalysis* **2**, 659–670 (2019).
30. Ohno, K. & Maeda, S. Global reaction route mapping on potential energy surfaces of formaldehyde, formic acid, and their metal-substituted analogues. *Journal of Physical Chemistry A* **110**, 8933–8941 (2006).
31. Maeda, S., Ohno, K. & Morokuma, K. Systematic exploration of the mechanism of chemical reactions: The global reaction route mapping (GRRM) strategy using the ADDF and AFIR methods. *Physical Chemistry Chemical Physics* **15**, 3683–3701 (2013).
32. Maeda, S., Komagawa, S., Uchiyama, M. & Morokuma, K. Finding reaction pathways for multicomponent reactions: The passerini reaction is a four-component reaction. *Angewandte Chemie - International Edition* **50**, 644–649 (2011).
33. Maeda, S., Taketsugu, T., Ohno, K. & Morokuma, K. From Roaming Atoms to Hopping Surfaces: Mapping Out Global Reaction Routes in Photochemistry. *J Am Chem Soc* **137**, 3433–3445 (2015).
34. Maeda, S., Harabuchi, Y., Ono, Y., Taketsugu, T. & Morokuma, K. Intrinsic reaction coordinate: Calculation, bifurcation, and automated search. *International Journal of Quantum Chemistry* **115**, 258–269 (2015).
35. Maeda, S., Sugiyama, K., Sumiya, Y., Takagi, M. & Saita, K. Global reaction route mapping for surface adsorbed molecules: A case study for H2O on Cu(111) surface. *Chemistry Letters* **47**, 396–399 (2018).
36. Sugiyama, K., Sumiya, Y., Takagi, M., Saita, K. & Maeda, S. Understanding CO oxidation on the Pt(111) surface based on a reaction route network. *Physical Chemistry Chemical Physics* **21**, 14366–14375 (2019).

37. Yoshimura, T. *et al.* Exploring the full catalytic cycle of rhodium(i)-BINAP-catalysed isomerisation of allylic amines: A graph theory approach for path optimisation. *Chemical Science* **8**, 4475–4488 (2017).
38. Maeda, S. *et al.* Implementation and performance of the artificial force induced reaction method in the GRRM17 program. *Journal of Computational Chemistry* **39**, 233–250 (2018).
39. Hayashi, H. *et al.* Synthesis of Difluoroglycine Derivatives from Amines, Difluorocarbene, and CO_2: Computational Design, Scope, and Applications. *Chemistry - A European Journal* 1–9 (2021) doi:10.1002/chem.202100812.
40. Mita, T., Harabuchi, Y. & Maeda, S. Discovery of a synthesis method for a difluoroglycine derivative based on a path generated by quantum chemical calculations. *Chemical Science* **11**, 7569–7577 (2020).
41. Sugiyama, K., Saita, K. & Maeda, S. A reaction route network for methanol decomposition on a Pt(111) surface. *Journal of Computational Chemistry* **42**, 2163–2169 (2021).
42. Oyama, S. T. Chemical and Catalytic Properties of Ozone. *Catalysis Reviews - Science and Engineering* **42**, 279–322 (2000).
43. Sugasawa, M. & Ogata, A. Effect of different combinations of metal and zeolite on ozone-assisted catalysis for toluene removal. *Ozone: Science and Engineering* **33**, 158–163 (2011).
44. Kim, H. H. *et al.* Ozone-assisted catalysis of toluene with layered ZSM-5 and Ag/ZSM-5 zeolites. *Plasma Chemistry and Plasma Processing* **33**, 1083–1098 (2013).
45. Chao, C. Y. H., Kwong, C. W. & Hui, K. S. Potential use of a combined ozone and zeolite system for gaseous toluene elimination. *Journal of Hazardous Materials* **143**, 118–127 (2007).
46. Xi, Y., Reed, C., Lee, Y. K. & Oyama, S. T. Acetone oxidation using ozone on manganese oxide catalysts. *Journal of Physical Chemistry B* **109**, 17587–17596 (2005).
47. Reed, C., Xi, Y. & Oyama, S. T. Distinguishing between reaction intermediates and spectators: A kinetic study of acetone oxidation using ozone on a silica-supported manganese oxide catalyst. *Journal of Catalysis* **235**, 378–392 (2005).
48. Einaga, H. & Futamura, S. Catalytic oxidation of benzene with ozone over alumina-supported manganese oxides. *Journal of Catalysis* **227**, 304–312 (2004).
49. Einaga, H., Maeda, N. & Teraoka, Y. Effect of catalyst composition and preparation conditions on catalytic properties of unsupported manganese oxides for benzene oxidation with ozone. *Applied Catalysis B: Environmental* **142–143**, 406–413 (2013).
50. Božović, A. *et al.* Conversion of methane to methanol: Nickel, palladium, and platinum (d 9) cations as catalysts for the oxidation of methane by ozone at room temperature. *Chemistry - A European Journal* **16**, 11605–11610 (2010).
51. McDonald, D. C. *et al.* Temperature and Isotope Dependent Kinetics of Nickel-Catalyzed Oxidation of Methane by Ozone. *Journal of Physical Chemistry A* **122**, 6655–6662 (2018).
52. Dillemuth, F. J., Skidmore, D. R. & Schubert, C. C. The reaction of ozone with methane. *Journal of Physical Chemistry* **64**, 1496–1499 (1960).
53. Hui, K. S., Kwong, C. W. & Chao, C. Y. H. Methane emission abatement by Pd-ion-exchanged zeolite 13X with ozone. *Energy and Environmental Science* **3**, 1092–1098 (2010).

54. Keenan, M., Nicole, J. & Poojary, D. Ozone as an Enabler for Low Temperature Methane Control Over a Current Production Fe-BEA Catalyst. *Topics in Catalysis* **62**, 351–355 (2019).
55. Jin, S. M., Lee, K. Y. & Lee, D. W. Ozone-induced lean methane oxidation over cobalt ion-exchanged BEA catalyst under dry reaction conditions. *Journal of Industrial and Engineering Chemistry* **112**, 296–306 (2022).
56. Ito, Y. Methane purification method and Methance purification system. JPA P2017-170309A (2017).
57. Wan, M. P., Hui, K. S., Chao, C. Y. H. & Kwong, C. W. Catalytic combustion of methane with ozone using Pd-exchanged zeolite X: Experimental investigation and kinetics model. *Combustion Science and Technology* **182**, 1429–1445 (2010).
58. Liu, C., Tranca, I., van Santen, R. A., Hensen, E. J. M. & Pidko, E. A. Scaling Relations for Acidity and Reactivity of Zeolites. *Journal of Physical Chemistry C* **121**, 23520–23530 (2017).
59. Sandoval-Díaz, L. E., González-Amaya, J. A. & Trujillo, C. A. General aspects of zeolite acidity characterization. *Microporous and Mesoporous Materials* **215**, 229–243 (2015).
60. Farneth, W. E. & Gorte, R. J. Methods for Characterizing Zeolite Acidity. *Chemical Reviews* **95**, 615–635 (1995).
61. Perdew, J. P., Burke, K. & Ernzerhof, M. Generalized Gradient Approximation Made Simple. *Physical Review Letters* **77**, 3865–3868 (1996).
62. Kresse, G. & Hafner, J. Ab initio molecular dynamics for open-shell transition metals. *Physical Review B* **48**, 13115–13118 (1993).
63. Kresse, G. & Hafner, J. Ab initio molecular-dynamics simulation of the liquid-metal–amorphous-semiconductor transition in germanium. *Physical Review B* **49**, 14251–14269 (1994).
64. Blöchl, P. E. Projector augmented-wave method. *Physical Review B* **50**, 17953–17979 (1994).
65. Kresse, G.; Joubert, D., Kresse, G. & Joubert, D. From ultrasoft pseudopotentials to the projector augmented-wave method. *Physical Review B* **59**, 1758–1775 (1999).
66. Monkhorst, H. J. & Pack, J. D. Special points for Brillouin-zone integrations. *Physical Review B* **13**, 5188–5192 (1976).
67. Grimme, S., Ehrlich, S. & Goerigk, L. Effect of the damping function in dispersion corrected density functional theory. *Journal of Computational Chemistry* **32**, 1456–1465 (2011).
68. Baerlocher, C.; McCusker, L. B.; van Koningsveld, H. Database of Zeolite Structures; http://www.iza-structure.org/databases/ (accessed Jun. 2021).
69. Fukui, K. The Path of Chemical Reactions — The IRC Approach. *Accounts of Chemical Research* **14**, 363 (1981).

Author Information

Corresponding author

Ken-ichi Shimizu - Institute for Catalysis, Hokkaido University, N-21, W-10, Sapporo 001-0021, Japan;
Email: kshimizu@cat.hokudai.ac.jp

Orcid: http://orcid.org/0000-0003-0501-0294

Authors

Shunsaku Yasumura - Institute for Catalysis, Hokkaido University, N-21, W-10, Sapporo 001-0021, Japan.
Orcid: https://orcid.org/0000-0002-4951-186X
Kenichiro Saita - Department of Chemistry, Faculty of Science, Hokkaido University, Sapporo, Hokkaido 060-0810, Japan.
Orcid: https://orcid.org/0000-0001-7705-5833
Takumi Miyakage - Institute for Catalysis, Hokkaido University, N-21, W-10, Sapporo 001-0021, Japan.
Kenichi Kon - Institute for Catalysis, Hokkaido University, N-21, W-10, Sapporo 001-0021, Japan.
Takashi Toyao - Institute for Catalysis, Hokkaido University, N-21, W-10, Sapporo 001-0021, Japan;
Orcid: http://orcid.org/0000-0002-6062-5622
Zen Maeno - School of Advanced Engineering, Kogakuin University, Tokyo, 192-0015, Japan
Orcid: https://orcid.org/0000-0002-9300-219X
Tetsuya Taketsugu - Department of Chemistry, Faculty of Science, Hokkaido University, Sapporo, Hokkaido 060-0810, Japan; Institute for Chemical Reaction Design and Discovery (WPI-ICReDD), Hokkaido University, Sapporo, Hokkaido 001-0021, Japan.
Orcid: https://orcid.org/0000-0002-1337-6694

ACKNOWLEDGMENT

This research was financially supported by JST-CREST (JPMJCR17J3) and JSPS KAKENHI (21H04626) grants. Some of the calculations were conducted employing the supercomputing resources at the Cyberscience Center of Tohoku University. S.Y. is grateful to the MANABIYA system of the Institute for Chemical Reaction Design and Discovery (ICReDD) of Hokkaido University, which was established by the World Premier International Research Initiative (WPI), MEXT, Japan, to support the learning of the GRRM program techniques for DFT calculations. This research is one of the projects promoted by the Research Association of Automotive Internal Combustion Engines (AICE) and is financially supported by the Japan Ministry of Economy, Trade, and Industry. The authors acknowledge the Technical Division of the Institute for Catalysis of Hokkaido University. S.Y. acknowledges the Grant-in-Aid for JSPS Fellows (21J11744, DC2).

Author contributions:

S.Y. wore the draft and carried out DFT calculations as well as the most of experiments. K.Saita and T.Taketsugu deeply discussed the applied computational approach and critically supported to utilize GRRM program. T.M. conducted the kinetic analysis for CH_4 combustion reaction. K.K. prepared the catalysts and performed NH_3 adsorption measurement. K.Saita, T.Taketsugu, T.Toyao and Z.M. critically revised the manuscript. K.Shimizu designed and supervised the whole project.

Competing interest statement

The authors declare no competing interests.

Figure Legends

Fig. 1 Rational design concept for catalytic combustion of CH_4 with O_3. (a) Employing single-component (SC)-AFIR, CH_4 combustion with O_3 was comprehensively explored to determine the key intermediates and elementary steps. (b) Different active sites were evaluated regarding the decrease in *Ea* of the key elementary step. (c) Heterogeneous catalyst comprising the predicted active site was tested experimentally.

Fig. 2 (a) Calculated reaction pathway of $CH_4 + O_3$, as well as the values of relative energies (ΔEs). The values written in dark red represent *Ea*. (b) Energy profile of CH_4 combustion to yield CO_2. The reaction path shown by the red lines is the most plausible for CO_2 formation. The results of the Bader charge analyses of the TS structures of $CH_4 + O_3$ and $CH_3OH + O_3$ are shown together. ΔEs are provided under each bar, and the *Ea*s are described employing the bold italic style (Unit: kJ/mol)

Fig. 3 Calculated reaction pathways of $CH_4 + O_3$ on (a) Cu(0) atom, (b) NO molecule, (c) C_5H_5N molecule, and (d) H_2SO_4 molecule. The values of ΔE and the *Ea* (dark red) are shown together (Unit: kJ/mol)

Fig. 4 (a) Employed periodic model of the ß zeolite. (b) Structure of the adsorption of C_5H_5N on BAS of ß zeolite. (c) TS calculations of the $CH_4 + O_3$ reaction on BAS of the ß zeolite. ΔE is reported in the kJ/mol unit. *Ea* is shown in dark red. (d) Plot of *Ea* of the $CH_4 + O_3$ reaction as a function of the C_5H_5N-stabilization energy (E_{pyr}) of the acids. (e) CH_4 conversion of 40 mg of the samples in 0.1% CH_4 + 5.95% O_2 + 0.7% O_3 + 3% H_2O at 200 °C (He balance, total flow: 100 ml/min) as a function of E_{pyr}

Fig. 5 (a) CH_4 and (b) O_3 conversions over 40 mg of the Hß zeolite with an Si/Al ratio of 8.5 (Hß8.5) and 40 mg of 5 wt% Pd-loaded Al_2O_3 (Pd5Al_2O_3) in 0.1% CH_4 + 5.95% O_2 + 0.7% O_3 and 0.1% CH_4 + 10% O_2 flows as functions of the reaction temperature. (c) Conversions of CH_4 and O_3 over 40 mg of the Hß zeolite with different Si/Al ratios (8.5, 12.5, 20, and 255) in a 0.1% CH_4 + 5.95% O_2 + 0.7% O_3 flow at 150 °C, together with the amount of BAS in the ß zeolite, as evaluated via NH_3-adsorption measurements. (d) Arrhenius plots for the combustions of CH_4 over Hß8.5 in 0.1% CH_4 + 5.95% O_2 + 0.7% O_3 at 160–190 °C, as well as over Pd5Al_2O_3 in 0.1% CH_4 + 10% O_2 at 170–220 °C. The reaction rates (V_{CH4}) at 190 °C over Hß8.5 and Pd5Al_2O_3 are shown together (R^2 = 0.99 for both catalyst). (e) Time course of CH_4 conversion over 40 mg of Pd5Al_2O_3 (at 400 °C) and Hß8.5 (at 200 °C) in 0.1% CH_4 + 3% H_2O + 40 ppm SO_2 + 10% O_2 or 5.95% O_2 +0.7% O_3 for Pd5Al_2O_3 and Hß8.5, respectively, with He balance (total flow: 100 ml/min). (f) Long-term reaction test for 10 mg of Hß8.5 in 0.1% CH_4 + 5.95% O_2 + 0.7% O_3 + 3% H_2O + 40 ppm SO_2 at 200 °C